A Numerical Study of a Sea Breeze at Fuerteventura Island, Canary Islands, Spain

Luis Cana · Diana Grisolía-Santos · Alonso Hernández-Guerra

Abstract The genesis and evolution of a sea-breeze front associated with a shallow convection episode at Fuerteventura Island (Canaries archipelago) are investigated using the Weather Research and Forecasting (WRF) numerical model. Three local and two non-local planetary boundary layer (PBL) parametrization schemes are used, and results of the numerical simulations are compared with observations from the local meteorological surface station network. Statistical analysis shows a good agreement between simulations and measurements, in particular for the 2-m temperature. These results are used in choosing the final PBL scheme and its coupled surface-layer scheme, which is used to simulate the daytime period of the sea-breeze development and weakening. During this episode, a sea-breeze front moved inland against a prevailing offshore flow three hours after sunrise, colliding with a downslope flow near the centre of the island. The convergence of both flows from opposing directions produced a strong updraft, forming shallow convection a few hours later.

Keywords Coastal meteorology · Planetary boundary-layer schemes · Sea-breeze front · Sea-breeze modelling · Weather Research and Forecasting model

1 Introduction

Sea breezes form part of local circulation cells driven by differential heating between land and sea. The basic dynamics and properties of these thermally-driven systems have been studied extensively since the 1950s and are generally well understood (Miller et al. 2003). One of the main components of the sea-breeze system is the frontal edge of the flow of cool moist marine air, usually termed the sea-breeze front (SBF). This element is associated with a marked temperature contrast and can resemble a synoptic-scale cold front.

✉ Luis Cana
luis.cana@ulpgc.es

Unidad de Océano y Clima, Instituto de Oceanografía y Cambio Global, IOCAG, Universidad de Las Palmas de Gran Canaria, ULPGC, Unidad Asociada ULPGC- CSIC. 35017 Las Palmas de Gran Canaria, Spain.

The dynamics of the sea breeze have been modelled extensively. Initially, the sea breeze was modelled in the context of linear theory (Dalu and Pielke 1989), although Rotunno (1983) stated that the nature of the different solutions depends on latitude, with closed circulations occurring only at latitudes greater than 30º, and wave patterns at latitudes of less than 30º. More recently, Qian et al. (2012) proposed an extension of the theory to include the effect of inland mountain ranges on the sea-breeze response.

The role of the sea-breeze circulation in triggering local convection has long been studied as well (see Dailey and Fovell 1999; Fovell and Dailey 2001), and studies on the Iberian Peninsula have shown how the SBF can modulate convection along the Mediterranean coast (Azorin-Molina et al. 2015), the Cantabrian coast of Spain (Arrillaga et al. 2016), and the Brittany coast of France (Calmet et al. 2018). All of these studies fall within the mid-latitude range and examine the development of sea breezes applied to continental terrain. Other studies have been conducted on islands with mountainous terrain in tropical latitudes, including Hawaii (Smolarkievicz et al. 1998), Dominica (Wang and Kirshbaum 2015), and Hainan (Huang et al. 2016) with the objective of determining the behaviour of sea breezes and their spatiotemporal evolution. Recently, idealized simulations have been carried out to study the impact of island terrain on sea-breeze circulations and how this affects the development of the SBF (Wang and Kirshbaum 2017).

However, the combination of shallow convection triggered by sea breezes close to a mountainous range at approximately 30º latitude has, to the best of our knowledge, yet to receive academic attention. In addition, potential interactions with the trade-wind inversion, which limits free convection, must be taken into account. Therefore, our aim here is to investigate how the sea-breeze circulation develops in an opposite direction to the prevailing flow, and how it evolves during the day along the eastern margin of the subtropical North Atlantic Ocean. To achieve this aim, we analyze an episode of shallow convection triggered by a sea breeze along the coast of Fuerteventura Island, Canaries archipelago, on 10 April 2007. This was an unusual day, with a surface west-north-west flow instead of the conventional trade winds (north-east). Both the European Centre for Medium-Range Weather Forecast (ECMWF) model and the operational HIRLAM model from the Spanish Meteorological Agency (Instituto Nacional de Meteorología, INM) failed to predict the development of shallow convection related to the sea-breeze episode, hence it deserves special attention.

The article is organized as follows: the next section describes the experimental design. In Sect. 3, we describe the results of the numerical tests using different settings of the Weather Research and Forecasting (WRF) model, in an attempt to match the observations obtained by three weather stations on Fuerteventura Island, as well as the simulation results using the optimal combination of available parametrizations. We then present a summary with a discussion in Sect. 4.

2 Description of the Numerical Experiment

The numerical simulations were carried out using the WRF model (version 3.9.1) developed at the National Center for Atmospheric Research (Skamarock et al. 2008). This model consists of fully compressible non-hydrostatic equations and has been extensively used for a variety of sea-breeze studies (see, for example, Tymvios et al. 2018; Hughes and Veron 2018; Lombardo et al. 2018) and planetary boundary-layer (PBL) studies (Jousse et al. 2016; Dimitrova et al. 2016; Banks et al. 2016; Ferrero et al. 2018).

2.1 Model Configuration

We used three nested domains in our set-up, performing the simulations by applying a 'two-way' nesting approach on the three modelled domains. Even when uncertainty exists regarding whether to use one-way or two-way nesting (Soriano et al., 2004), most recent sea-breeze simulations (Arrillaga et al. 2016, Dandou et al. 2017, Tymvios et al. 2018, Hughes and Veron 2018) have opted for the latter approach, and accordingly so did we.

The topography used was the GTOPO30 dataset at 30 s along with USGS24 land-category data and 16 soil categories, all retrieved from the archives of the United States Geological Survey (USGS). All domains were centred on the Fuerteventura Airport meteorological station, with the aim of representing regional-scale circulation around Fuerteventura Island as well as resolving the sea-breeze regime in this area. The three domains are located at the eastern boundary of the subtropical North Atlantic Ocean. A climate overview of this area can be found in Carrillo et al. (2016).

The coarse domain (30 × 24 points, 18.0 km grid spacing) covers the eastern islands of the Canaries archipelago and part of the north-west African coast, with the aim of capturing the synoptic and mesoscale features.

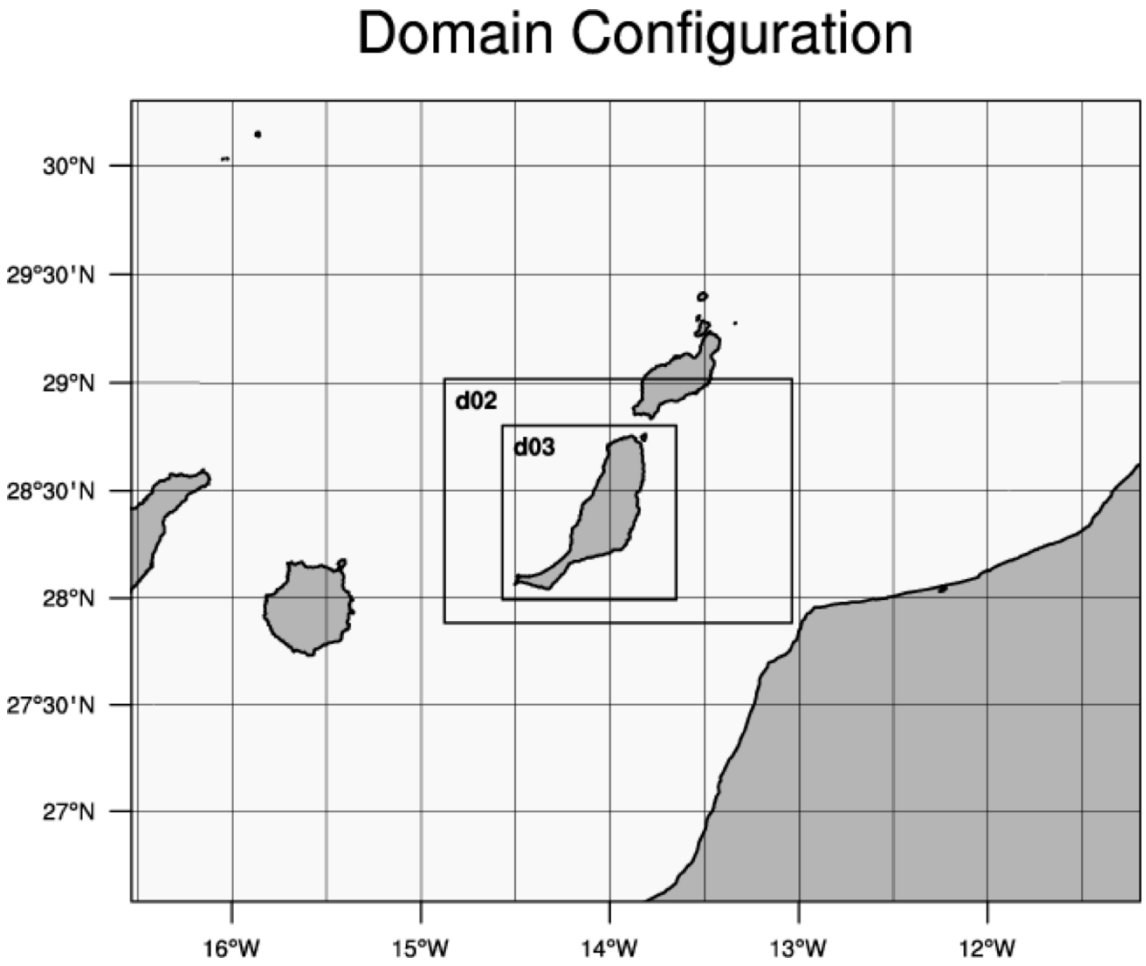

Fig. 1 Weather Research and Forecasting (WRF) model domains used in this study. Frames indicate the coarse grid as well as the two inner domains

Within domain 1, domain 2 (31 × 22 points, 6.0 km grid spacing) is nested covering both Fuerteventura Island and the south of Lanzarote Island, in order to include possible flow channelling across the strait (see Fig. 1). Finally, a fine-grid simulation (domain 3; 46 × 46 points, 2.0 km grid spacing) covers the island of Fuerteventura, with this last domain, as well as the terrain height, shown in Fig. 2. Fuerteventura Island is about 100 km long and 30 km wide, with its highest peak, Pico de la Zarza, located on the south-western end of the island on the Jandía Peninsula (see Fig. 2). Due to its size, it should be categorized as a small island (<150 km). According to Xian and Pielke (1991), or more recently Huang et al. (2016), the contrast between land and sea might be too small to develop deep mesoscale circulations, resulting instead in weak sea-breeze systems.

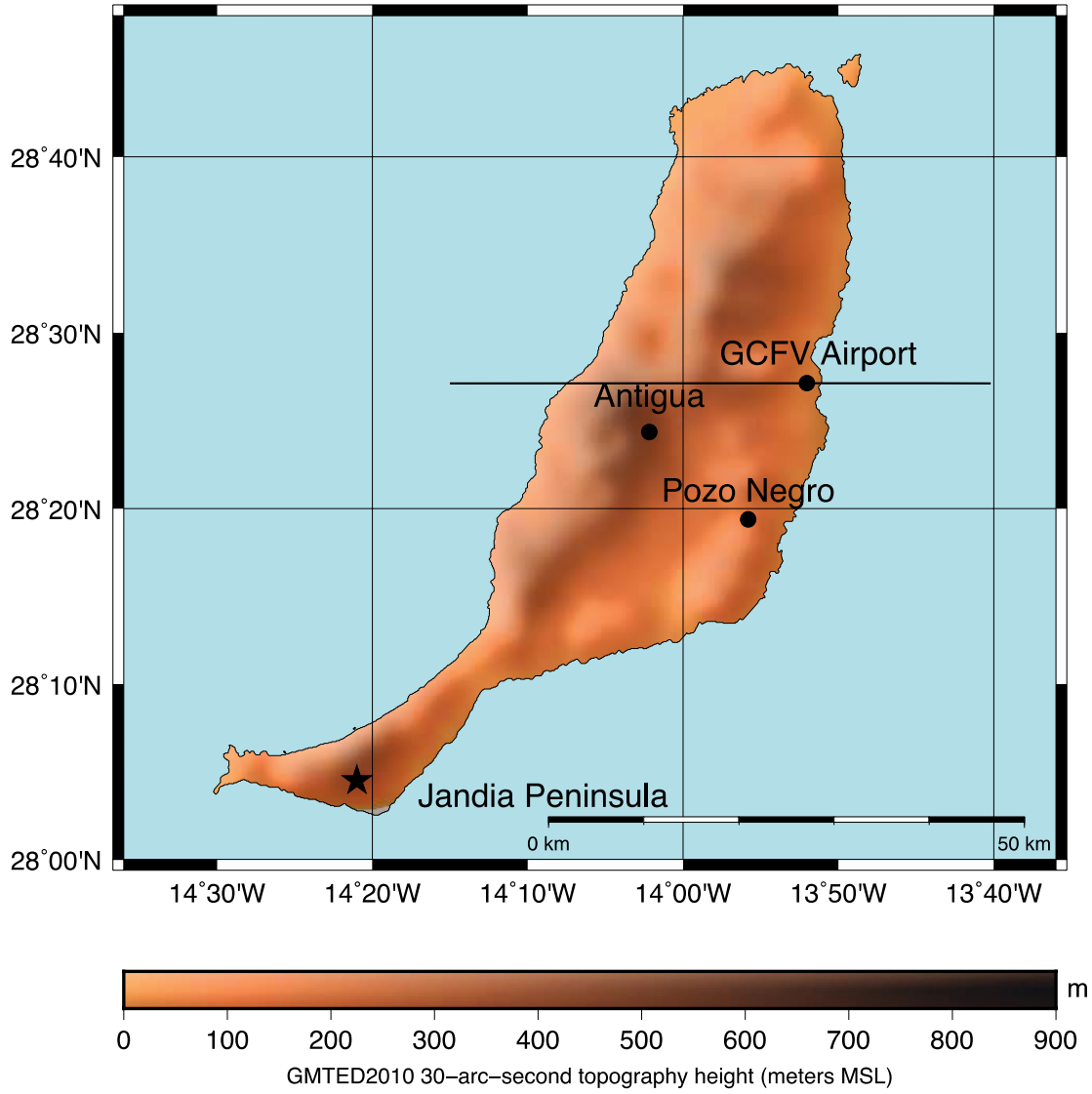

Fig. 2 Inner domain (D03) with the location of weather stations and the terrain height of the island of Fuerteventura. The highest peak is located in the south-western corner on the Jandía Peninsula (Pico de la Zarza; 807 m). The solid line represents a cross-section taken to analyze the vertical structure of the sea breeze

In our simulation, the model uses fifty terrain-influenced coordinate levels featuring a parabolic profile to resolve the atmosphere for all domains (model top at 50 hPa). The lowest level is at 20 m above mean sea level (a.s.l.), with the spacing between levels ranging from 60 m near the bottom, around 300 m in the middle and upper troposphere, to 400 m towards the top. Twenty-five levels are placed below 3 km in height in order to enhance the vertical resolution and thus better depict the PBL. The eta-levels of the vertical profile can be found in Table 2.

2.2 Initial and Boundary Conditions

All the simulations use the same initial and boundary conditions as derived from the ECMWF ERA-Interim Global Reanalysis data[1]. These are global data based on observations with a 0.7º horizontal grid mesh.

These analyses are interpolated to the WRF model grid to provide the initial conditions for 1200 UTC 9 April 2007, as well as six-hourly lateral boundary conditions for the 18.0 km domain. Following the Huang et al. (2016) method, the model simulation over domain 1 start at 1200 UTC 9 April 2007, ending at 0000 UTC 11 April 2007. Model simulations for domains 2 and 3 begin 12 h later, starting at 0000 UTC 10 April 2007 and ending at 0000 UTC 11 April 2007. Thus, the first 12 h are considered to be spin-up and the remainder are used for the analysis. The integration timestep of the coarser domain is 30 s, and decreased by a factor of three for the two nested domains.

Finally, the sea-surface temperature (SST) data are taken from the NASA MODIS aqua satellite imagery[2] as a boundary condition for the model. The SST was 19.3º C across the Canary Archipelago on this day, which is almost the mean value for the month (Hernández-Guerra et al., 2002).

2.3 Parametrization Schemes

WRF model dynamic and physical options used for all domains include the WRF Advanced Research (ARW) dynamic core, the Rapid Radiative Transfer Model (RRTM) for longwave and shortwave radiation (Mlawer et al. 1997), and the Grell-Dèvènyi 3D scheme (Grell and Dévényi 2002) cumulus parametrization, except for the inner domain. This cumulus scheme is designed for high-resolution simulations and may be used when the grid spacing is below 10 km, but due to the inner domain resolution (domain 3, 2 km) there is no need to apply any cumulus parametrization.

The PBL is directly influenced by the surrounding surface, for both land terrain and ocean. Stull (1991) stated that a non-local approach could better explain the

[1] European Centre for Medium-Range Weather Forecasts (2009): ERA-Interim Project. Research Data Archive at the National Center for Atmospheric Research, Computational and Information Systems Laboratory. Dataset. https://doi.org/10.5065/D6CR5RD9. Accessed† 29 May 2017

[2] NASA Goddard Space Flight Center, Ocean Ecology Laboratory, Ocean Biology Processing Group. Moderate-resolution Imaging Spectroradiometer (MODIS) Aqua Sea Surface Temperature Data; 2014 Reprocessing. NASA OB. DAAC, Greenbelt, MD, USA. doi:data/10.5067/AQUA/MODIS/L3B/SST/2014. Accessed on 23 May 2017

characteristics of the PBL above a forest canopy, whereas a local viewpoint could be inappropriate. A similar conclusion was reached in two convective boundary-layer cases over the Great Plains in the USA (Gibbs et al. 2011), where the non-local schemes gave results closer to observations, although the differences among local and non-local schemes were relatively small.

However, studies evaluating PBL schemes in the WRF model above oceans are characterized by notable discrepancies between them. Studies performed across Japan (Kwun et al. 2009) and over the North Sea (Nunalee and Basu 2014) have revealed that the marine boundary layer (MBL) is especially sensitive to the choice of PBL parametrization scheme. Arrillaga et al. (2016) have emphasized the importance of the careful selection of the PBL scheme to reproduce the sea-breeze phenomenon. Despite this, the comparison of several PBL schemes along the California Coast (Yver et al. 2013) and the Mediterranean Sea (Dandou et al. 2017) showed that the basic atmospheric parameters presented no major differences regarding the choice of PBL scheme, and none of the tested PBL schemes adequately simulated all PBL characteristics.

Given that the aforementioned studies were undertaken in mid-latitudes or tropical zones, one should consider whether these findings are valid for a subtropical zone such as the Canary Archipelago. Thus, we have chosen five common PBL parametrization schemes for testing: two first-order non-local closure schemes and three 1.5-order local closure schemes, summarized in Table 1.

Table 1 The PBL parametrization schemes tested in the WRF model

Local	Non-local
Mellor–Yamada–Janjic (MYJ) (Janjić 1994)	Yonsei University (YSU) (Hong et al. 2006)
Mellor–Yamada-Nakanishi–Niino (MYNN 2.5) (Nakanishi and Niino 2006)	Asymmetric Convective Model Version 2 (ACM2) (Pleim and Xiu 1995; Pleim 2007)
Grenier–Bretherton–McCaa (GB) (Grenier and Bretherton 2001)	

Given the possible high impact that parametrization schemes exert on the simulations, we have used the same radiation (longwave and shortwave), cumulus, and microphysical schemes, as well as the same initial and boundary conditions. Also, the same land-surface model (Noah/UCM) is applied to all PBL schemes except for the Asymmetric Convective Model Version 2 scheme (ACM2), which is only compatible

with the Pleim–Xiu land-surface scheme. Finally, several of the selected PBL schemes are tied to a particular surface-layer scheme and, therefore, it is not possible to have a common surface-layer scheme for all simulations. Thus, the Mellor–Yamada–Nakanishi–Niino 2.5 PBL model (MYNN) applies its own scheme, whereas the revised Penn State/NCAR Mesoscale Model version 5 (MM5) (Jiménez et al. 2012) is applied to the rest. This information is summarized in Table 2.

Table 2 Physical parametrization schemes and vertical profile used in the tests

Land-surface model	Noah/UCM model (Chen and Dudhia 2001) (YSU, MYJ, MYNN, GB) Pleim–Xiu model (Pleim and Xiu 1995; Gilliam and Pleim 2010) (ACM2)
Longwave radiation	Rapid Radiative Transfer Model (RRTM). (Mlawer et al. 1997) All schemes
Shortwave radiation	Rapid Radiative Transfer Model (RRTM). (Mlawer et al. 1997) All schemes
Surface-layer scheme	Revised MM5 similarity (Jiménez et al. 2012) (YSU, MYJ, GB, ACM2) MYNN similarity (MYNN 2.5)
Cumulus parametrization	(Grell and Dévényi 2002) All schemes
Microphysical parametrization	(Lin et al. 1983) All schemes
Eta levels: 1.0000, 0.9947, 0.9895, 0.9843, 0.9790, 0.9739, 0.9684, 0.9626, 0.9564, 0.9498, 0.9426, 0.9348, 0.9262, 0.9167, 0.9062, 0.8946, 0.8816, 0.8671, 0.8509, 0.8330, 0.8130, 0.7909, 0.7667, 0.7402, 0.7116, 0.6809, 0.6483, 0.6141, 0.5785, 0.5419, 0.5047, 0.4672, 0.4299, 0.3931, 0.3570, 0.3220, 0.2883, 0.2560, 0.2253, 0.1963, 0.1690, 0.1435, 0.1171, 0.0952, 0.0753, 0.0571, 0.0407, 0.0257, 0.0122, 0.0000	

2.4 Observational Data

Observations of 10-m wind speed, wind direction, and 2-m temperature are compared with the model simulations. These observations are provided by three regular meteorological stations, two of them (Pozo Negro and Molino de Antigua) maintained by the Instituto Canario de Investigaciones Agrarias (ICIA, Gobierno de Canarias), and the third one owned by the Agencia Estatal de Meteorología (AEMET). The first meteorological station is located close to the seashore, inside Fuerteventura airport (28.444 N, 13.863 W; 25 m a.s.l., referred to as GCFV airport). The Pozo Negro station (28.334 N, 13.941 W; 120 m a.s.l.) is located several kilometres inland at the end of a valley, whereas the Molino de Antigua station (28.433 N, 14.012 W; 321 m a.s.l., referred

200 to as Antigua) is located near the central ridge of the island, at sufficient altitude and
201 distance from the coast to be only slightly affected by the inland penetration of sea
202 breezes. These stations are distributed across the island and may be considered valid in
203 depicting the hourly evolution of the sea breeze and its progression inland (Fig. 2). All of
204 the stations have a sampling time of 10 min, although half-hourly averages are given.
205 In addition, we used the rawinsonde data of the Guimar station (Sta. Cruz de Tenerife
206 Island) on 10 April 2007 at 1200 UTC to characterize the vertical structure of the
207 atmosphere and its stability. The dataset is available at the website maintained by the
208 University of Wyoming (http://weather.uwyo.edu/upperair/sounding.html). This is the
209 closest sounding station to Fuerteventura Island and the only source of data for the vertical
210 structure of the atmosphere due to the lack of other vertical profilers. The SkewtT-logP
211 diagram (Fig. 3) depicts the well-known vertical structure of the atmosphere over the sub-
212 tropical North Atlantic. It is characterized by the trade-wind inversion, which determines
213 the top of the MBL (Carrillo et al., 2016). For our case, this is dictated by a sharp increase
214 in temperature (1.5º C) at 2,586 m. The moisture inside the MBL ranges from 8.9 g kg^{-1}
215 at the surface to 5.5 g kg^{-1} at the base of the inversion. The PBL mixing ratio is of 8.1 g
216 kg^{-1}, falling to 1.1 g kg^{-1} in the dry, warm and stable air layers above. The sub-cloud layer
217 begins at 781 m a.s.l. (925 hPa), where the lifting condensation level (LCL) is 894 hPa
218 and a conditionally unstable cloud layer extends up to the beginning of the trade-wind
219 inversion (742 hPa, 2,586 m). Compared with the Dominica Experiment sounding plot
220 (Wang and Kirshbaum 2015, Fig. 2) this sub-cloud layer is deeper, but the mixing ratio
221 is much lower (8.1 g kg^{-1} compared to 14–16 g kg^{-1} in Dominica).

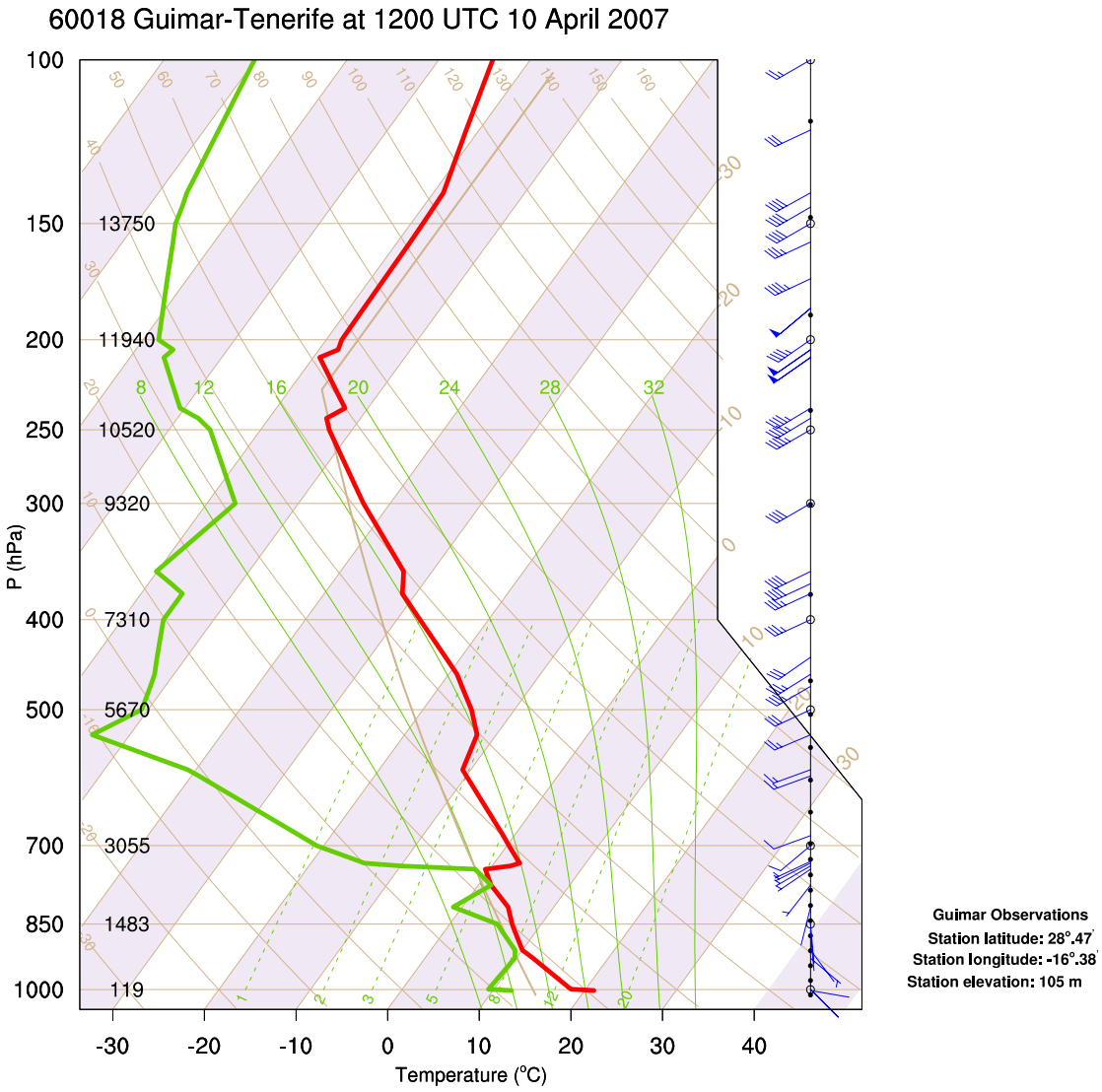

Fig. 3 SkewT-logP plot of the Guimar–Tenerife rawinsonde observations on 10 April 2007, 1200 UTC

3 Results and Discussion

3.1 Model Evaluation

We evaluate the WRF model performance by statistical analysis of the simulations related to the 10-m wind speed and 2-m temperature for the three ground stations. We calculated the averages of the simulated values for all variables to match the same period of observational data because the observations are given as half-hourly means, yielding a total of 32 samples. To describe the discrepancies between observations and simulated data, we use four statistical indices, including the mean bias error (*MBE*), root-mean-square error (*RMSE*), correlation coefficient (ρ), and index of agreement (*IA*). All of these are commonly used to evaluate the performance of models (Azorin-Molina et al. 2015,

Huang et al. 2016; Dandou et al. 2017); the relations used to calculate these statistical indicators can be found in the Appendix.

The 10-m wind speed is generally poorly simulated for weather stations located inland, and Table 3 summarizes the statistical analysis of the five PBL schemes for simulating the 10-m wind speed and direction.

Table 3 Statistical analysis of the 10-m wind speed and direction on 10 April 2007 from 0600–2200 UTC at the island of Fuerteventura during a sea-breeze episode, for (a) wind speed and (b) wind direction

a. speed							*b. direction*	
PBL	Station	Obs ($m\ s^{-1}$)	*MBE* ($m\ s^{-1}$)	*RMSE* ($m\ s^{-1}$)	ρ	*IA*	*MBE* (º)	*IA*
YSU	GCFV airport	2.3	0.7	0.8	0.88	0.84	-22	0.86
	Pozo Negro	2.4	0.4	1.5	0.20	0.42	23	0.52
	Antigua	2.4	0.2	1.0	0.52	0.71	128	0.49
ACM2	GCFV airport	2.3	0.8	1.1	0.92	0.80	-14	0.93
	Pozo Negro	2.4	0.5	1.5	0.22	0.44	18	0.51
	Antigua	2.4	-0.1	1.2	0.40	0.60	110	0.59
MYJ	GCFV airport	2.3	-0.1	0.6	0.81	0.89	07	0.88
	Pozo Negro	2.4	0.9	1.7	0.25	0.44	15	0.67
	Antigua	2.4	0.1	1.4	0.20	0.20	43	0.46
MYNN	GCFV airport	2.3	0.6	0.7	0.92	0.87	-09	0.99
	Pozo Negro	2.4	0.8	1.5	0.10	0.34	14	0.63
	Antigua	2.4	0.3	1.2	0.40	0.61	106	0.56
GB	GCFV airport	2.3	0.1	0.4	0.80	0.85	-09	0.83
	Pozo Negro	2.4	1.1	2.0	0.15	0.37	-06	0.37
	Antigua	2.4	0.1	1.4	0.11	0.31	52	0.70

Obs stands for the mean value of the observations

In terms of wind speed, all PBL schemes show positive *MBE* values except for two that are close to zero. The *RMSE* parameter gives a relatively high weight to large errors, registering the largest deviations at Pozo Negro station ($1.5 \leq RMSE \leq 2.0$). Both YSU and MYNN schemes give very similar results in *MBE* and *RMSE* values at GCFV airport, which indicates that at this location neither of these two schemes presents large errors. In this case, Antigua station exhibits better behaviour than Pozo Negro (lower *MBE* values), although occasionally there are important differences in wind speed ($1.0 \leq RMSE \leq 1.4$). The correlation coefficient indicates that there is a good fit only in the airport area (GCFV airport; $0.80 \leq \rho \leq 0.92$), being more accurate for the station located next to the mountain barrier (Antigua; $0.11 \leq \rho \leq 0.52$) than for the one placed inside a narrow valley (Pozo Negro; $0.10 \leq \rho \leq 0.25$). Finally, for all PBL schemes, the best

performance is achieved at the airport station (GCFV airport), where an $IA > 0.80$ is obtained in all cases. The *IA* parameter is a standardized measure of the degree of simulation error, and for both the inland stations, the *IA* analysis shows poor results, with $IA < 0.61$ for all schemes (in particular Pozo Negro $0.34 \leq IA \leq 0.44$) with the exception of YSU at Antigua station ($IA = 0.71$).

With regard to wind direction, half-hourly means were compared with observations from the ground stations. Only *MBE* was used to characterize the deviations and *IA* to check the degree of adjustment. *MBE* values are negative for the GCFV airport station for almost all PBL schemes and may show important deviations (up to 128º at Antigua; lower at Pozo Negro). On the other hand, *IA* values are high at GCFV airport ($0.86 \leq IA \leq 0.99$) and lower at Pozo Negro station ($0.37 \leq IA \leq 0.67$) and Antigua ($0.46 \leq IA \leq 0.70$). The discrepancy between *IA* and *MBE* can be related to the flow from the north affecting the statistical calculation (Buckley et al. 2004). In our case, this occurs during the onset and the dissipation of the breeze (see Fig. 4b). Moreover, the Pozo Negro station is located at the end of a narrow canyon, through which the flow is forced to follow a west-east direction. Given the size of the smallest mesh (2 km), the model is unable to capture this feature, and the simulated sea breeze runs along a wide valley in a south-west–north-east direction (see Fig. 2), thereby failing to fully reproduce both the true wind direction and speed. This behaviour also occurs at the Antigua station, which is located close to the main ridge of the island in an open area affected by downslope topographic flow (see Fig. 2). We attribute to the particular orographic conditions of the inland stations the inability of the model to fully reproduce the real flow, especially in terms of its direction. As noted by Dandou et al. (2017), PBL schemes cannot represent the variability of the observations and do not accurately predict wind fields.

Although no PBL scheme stands out in the 10-m wind simulation, non-local schemes (in particular YSU) seem to obtain reliable wind simulations, in agreement with previous studies (Cohen et al. 2015; Banks et al. 2016). Figure 4 shows a comparison of the different PBL schemes for simulating wind speed (Fig. 4a) and direction (Fig. 4b) at the GCFV airport station.

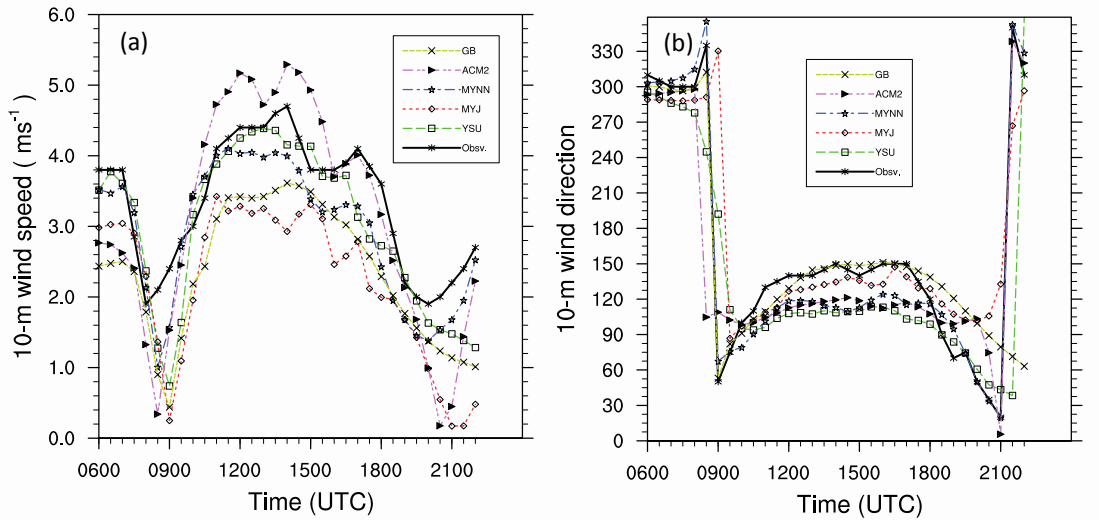

Fig. 4 (a) 10-m wind speed and, (b) 10-m wind direction for the GCFV airport weather station. The black line represents observations and the coloured lines show the results for the five tested PBL schemes

The results for the 2-m temperature show much better performances for all of the tested schemes, although the non-local schemes again represent the best performers. The statistical parameters are shown in Table 4, indicating a very good correlation between simulated and observed temperatures.

Table 4 As in Table 3, but for 2-m temperature

PBL	Station	Obs (ºC)	*MBE* (ºC)	*RMSE* (ºC)	ρ	*IA*
YSU	GCFV airport	19.4	-0.1	0.4	0.98	0.99
	Pozo Negro	19.4	-0.3	0.5	0.98	0.99
	Antigua	17.7	-0.1	0.8	0.92	0.96
ACM2	GCFV airport	19.4	0.6	1.1	0.90	0.91
	Pozo Negro	19.4	0.5	1.3	0.94	0.92
	Antigua	17.7	0.6	1.4	0.87	0.90
MYJ	GCFV airport	19.4	-1.0	1.7	0.94	0.60
	Pozo Negro	19.4	-0.8	1.7	0.86	0.67
	Antigua	17.7	0.6	1.6	0.88	0.91
MYNN	GCFV airport	19.4	-1.4	1.8	0.80	0.69
	Pozo Negro	19.4	-1.1	1.4	0.88	0.87
	Antigua	17.7	-1.6	2.3	0.60	0.69
GB	GCFV airport	19.4	-0.9	1.7	0.78	0.56
	Pozo Negro	19.4	-0.6	1.6	0.87	0.68
	Antigua	17.7	0.6	1.1	0.91	0.92

Obs stands for the mean value of the observations

In particular, both the Yonsei University (YSU) and ACM2 PBL schemes (non-local) performed very well in our test. Regarding the YSU results, the *MBE* parameter is slightly

302 negative for all three stations ($-0.3 \leq MBE \leq -0.1$; Table 4), with low *RMSE* values
303 (0.4 at GCFV airport) and a high correlation coefficient ($0.92 \leq \rho \leq 0.98$). The index
304 of agreement is very high, over 0.95 for the three locations ($0.96 \leq IA \leq 0.99$). These
305 results reveal that the PBL simulation using the YSU scheme is reliable and that there are
306 no values that significantly differ from those recorded at the stations. The performance of
307 the ACM2 PBL scheme is slightly worse, with positive values for both *MBE* ($0.5 \leq$
308 $MBE \leq 0.6$) and *RMSE* ($1.1 \leq RMSE \leq 1.4$).
309 However, all local schemes (MYJ, MYNN, and GB) clearly produce lower results
310 than those shown by the YSU or ACM2 PBL schemes. Thus, the MYNN scheme yields
311 negative *MBE* values ($-1.6 \leq MBE \leq -1.1$) and higher values of *RMSE* ($1.4 \leq$
312 $RMSE \leq 2.3$) than its local counterparts; moreover, both the correlation coefficient
313 ($0.60 \leq \rho \leq 0.88$) and the index of agreement ($0.69 \leq IA \leq 0.87$) are clearly worse.
314 Similar results are obtained for the MYJ and GB schemes. These 2-m temperature results
315 are in agreement with Huang et al. (2016) and Arrillaga et al. (2016), who concluded that
316 non-local schemes provided less biased temperatures over the subtropical Pacific, tropical
317 Atlantic, and north coast of the Iberian Peninsula than do local schemes.
318 Finally, we must have in mind that previous works (Jousse et al. 2016, Gunwani and
319 Mohan 2017) have argued that existing PBL parametrizations in the WRF model are
320 unable to produce fully accurate results. This behaviour is especially notable for locations
321 characterized by shallow cumulus regimes (Huang et al. 2013), a typical feature of the
322 weather on Fuerteventura Island and most of the Canary Archipelago (Carrillo et al.
323 2006). Considering our results and the findings of Jousse et al. and Gunwani and Mohan
324 as well as the limited temporal coverage of our test, we believe that our results are valid
325 for this particular episode, but need to be verified in other cases.
326
327 **3.2 Simulated Sea-Breeze Episode**
328 Attending both to the 10-m wind and 2-m temperature results, both the MYNN or the
329 YSU PBL schemes are suitable for simulating this sea-breeze episode, with the MYNN
330 scheme slightly better for the wind simulation and the YSU scheme clearly better for the
331 temperature simulation. Previous works have concluded that there is not a definitive
332 recommendation for the use of a specific scheme (Gibbs et al. 2011, Dandou et al. 2017),
333 although the YSU scheme usually performs better than the MYNN scheme (Smith et al.
334 2018). Bearing in mind the previous conclusions and following Arrillaga et al. (2016) and
335 Huang et al. (2016), we chose the YSU PBL scheme for the simulation of this sea-breeze

episode, as it is a non-local scheme with very high performance for simulating thermodynamic parameters, and is characterized by a good agreement between the simulated and observed wind for most of the available weather stations.

3.2.1 Spatial Variation

We use two plots to describe the evolution of this sea-breeze episode. The first one (left) combines the 10-m wind plot and the 2-m temperature to depict the main mechanism for sea-breeze generation, i.e., the differential heating of land and sea, forming a local circulation cell. The second plot (right) presents the PBL height, where the surface wind is overlain in order to show how the sea breeze influences the temporal evolution of the boundary layer. The PBL height is available from the model simulations and corresponds to the height above ground. Using the critical bulk Richardson number, the YSU scheme determines the PBL height, with a critical value of zero for an unstable boundary layer and 0.25 for a stable boundary layer (Hong et al. 2006).

Figure 5 depicts the conditions at dawn, when a general north-westerly flow occurs over Fuerteventura Island. For this particular day, there is a cross-barrier low-level flow, which is atypical (north-east trade winds; along-barrier flow). The land is cooler (15º C) than the surrounding ocean (19º C) as a result of nocturnal cooling. At this time, the highest wind speed is recorded in the lee of the island along its eastern coast (>5 m s^{-1}). The flow slows down to the west of the mountain range and accelerates downwind (Fig. 5a). The PBL is higher off the coast, and shows its minimum value over the island, where the nocturnal cooling turns the vertical profile in a stable atmospheric stratification. The PBL height is under 200 m, matching the typical value for this condition (Huang et al. 2016).

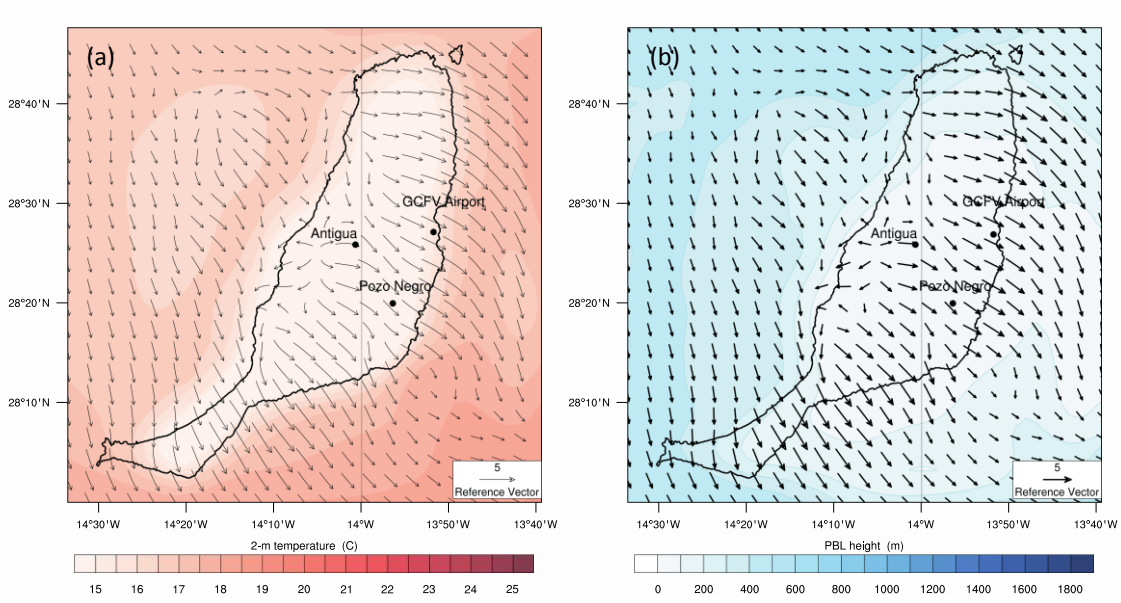

Fig. 5 Simulation images valid for 10 April 2007, 0600 UTC. (a) 2-m temperature and 10-m wind speed (m s^{-1}) at dawn. (b) 10-m wind speed (m s^{-1}) and PBL height

About three hours after sunrise, there is a significantly greater heating of the land, which begins to become warmer than the surrounding ocean. This differential heating starts to modify the main circulation, as the wind starts to change direction (veer) across the north-east of the island close to the airport station (GCFV airport in Fig. 6a), but also backs anticlockwise south of the Pozo Negro station. This behaviour matches the low-level winds undergoing convective evolution over a heated ridge described by Soderholm et al. (2014), where the windward flow converged with reversed lee-side flow downwind of the crest. There is also another change in the local flow around Pozo Negro, with a local flow from the south-west moving inland across a valley. The wind speed plot shows a decrease in speeds across much of the island (Fig. 6b), except for in its south-western part, where the channelling of flow across the isthmus located between the surrounding mountainous areas remains strong (>5 m s^{-1}) (see Fig. 2 for topography of Jandía Península). With the airflow from sea to land, the convective boundary layer starts to develop due to the change in the aerodynamic roughness and temperature between the two surfaces (Garratt 1990). This is clearly visible at the leeward side of the island where the PBL height can reach about 800–1000 m.

We attribute the stronger development of the PBL height at the leeward side to the differences in the sea-breeze development. The windward side of the island is characterized by an onshore flow, which advects cold air from the sea towards the coastal area. Thus, the thermal difference is less than on the leeward side, resulting in a weaker

sea breeze that penetrates inland close to the mountain range. However, the leeward side begins to develop the sea-breeze cell after the wind starts to change its direction. The heating of the inland area is stronger (especially near the valley at the south-west of Pozo Negro) and there is no advection of cold air, which may restrict the increase in air temperature. Accordingly, the PBL develops without restrictions, reaching higher levels.

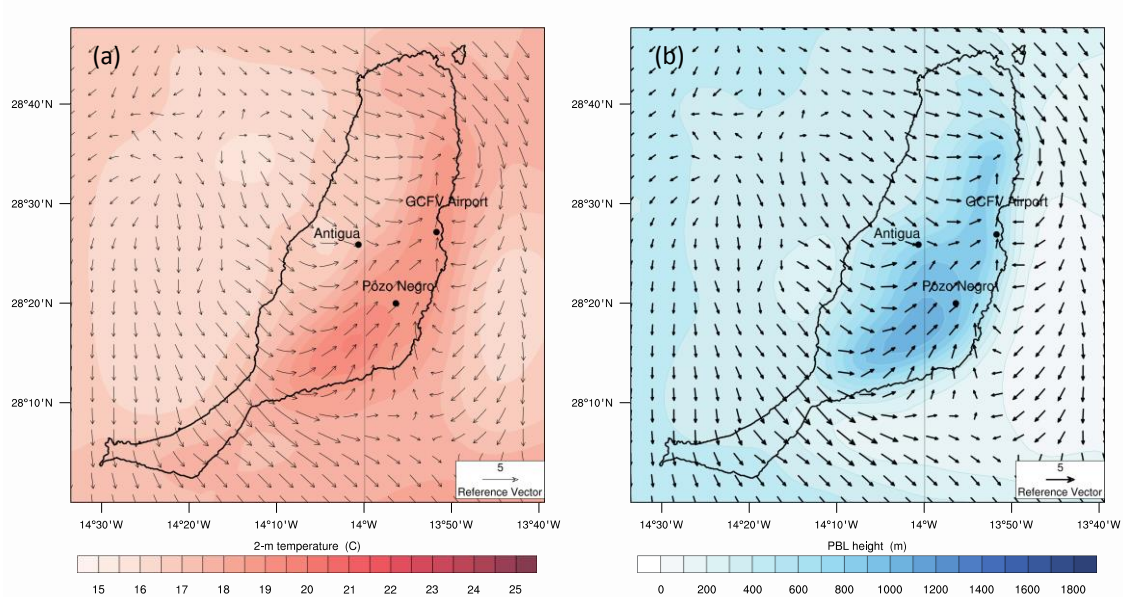

Fig. 6 Same as in Fig. 5, but for 0900 UTC

Figure 7 shows the maximum development of this sea-breeze episode a few hours after noon. Simultaneously with the maximum wind speed at the GCFV airport station (Fig. 4a), two opposing flows collide along the axis of the island, creating a convergence that generates an upward motion and consequently the onset of shallow convection that characterizes this episode. The 2-m temperature is clearly higher above the island (Fig. 7a) and the convergence of both opposing flows causes an updraft, which initiates shallow convection and the rise of the PBL along the island (Fig. 7b). At this moment, most of the PBL height over the island is well above 1,200 m, with two areas (south of Pozo Negro and north of GCFV airport) reaching 1,800 m. The location of the SBF and the extension of the inland flow can be placed along the axis of the island (north-east to south-west, marked as red solid lines), indicating that the sea breeze penetrates about 15 km inland from both sides, almost half the width of Fuerteventura. In order to reach this area, the sea breeze must flow from the coast to heights of about 300 m a.s.l.. Furthermore, the penetration inland of the cold marine air at the leeward side causes that the heating of the air of the coastal area to weaken, producing lower PBL heights than in areas located

inland. We should note that, despite the small size of the island, both the leeward and windward sea breezes are powerful enough to collide and develop a strong updraft, which should only be possible for medium-sized or large islands (Xian and Pielke 1991).

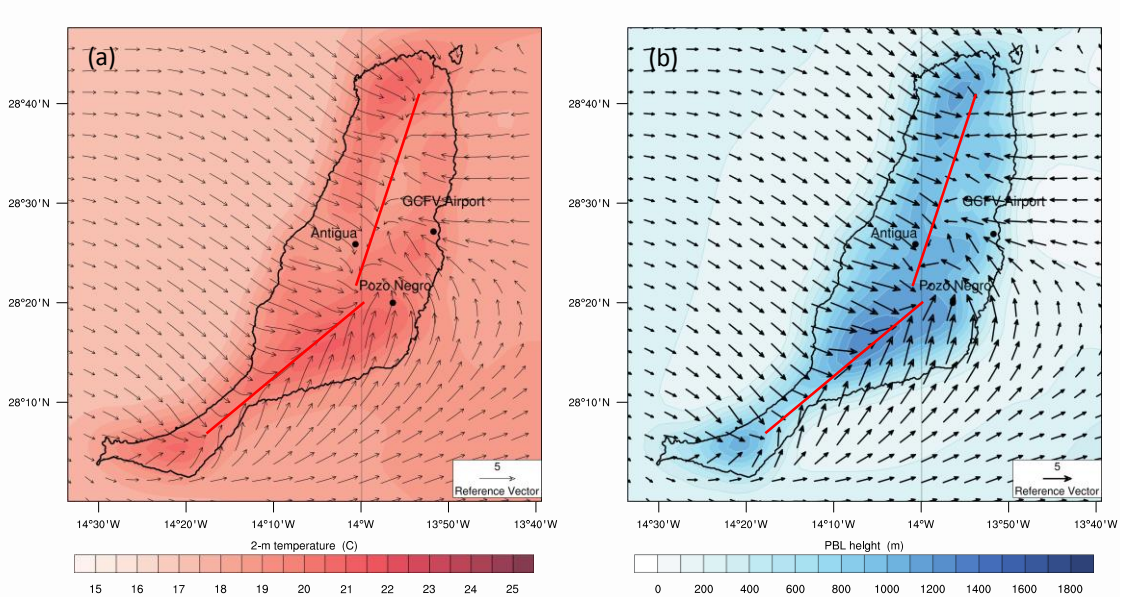

Fig. 7 Same as in Fig. 5, but for 1400 UTC. The solid lines depict the location of the SBF

Lastly, we present the final stage of the sea-breeze episode (Fig. 8), when the radiation balance starts to become negative and the land temperature begins to decrease at a faster rate than the surrounding sea (Fig. 8a). The wind turns again to the north-west and the local circulation adapts to this new situation. Consequently, the convection ceases and the PBL height over the island falls significantly (Fig. 8b) evolving again towards a stable atmospheric stratification over the land and showing heights of the same order as at the beginning of the process.

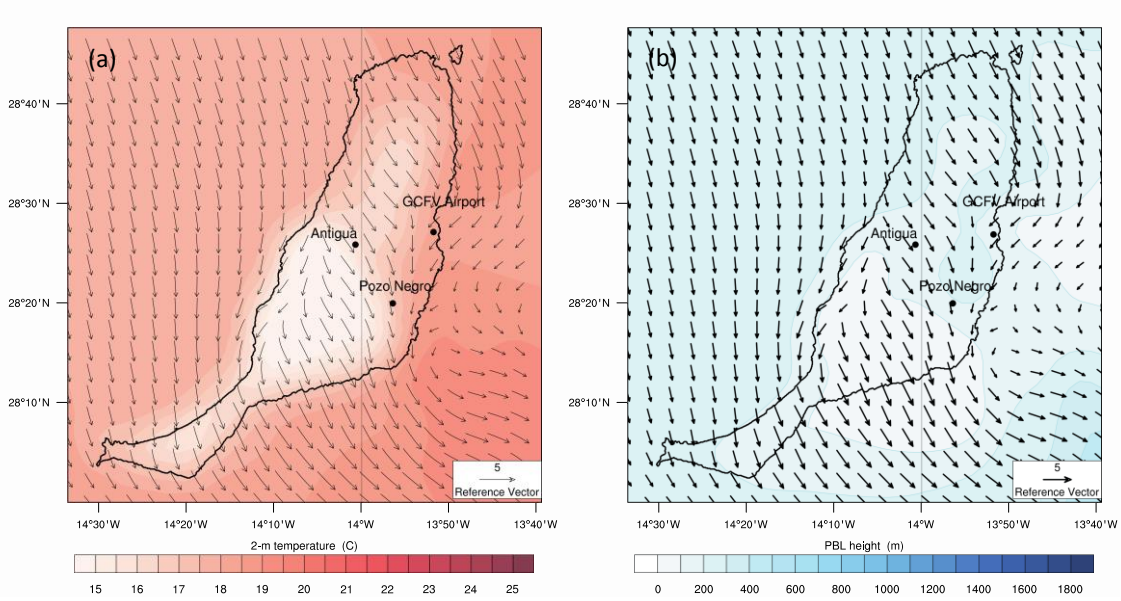

Fig. 8 Same as in Fig. 5, but for 2100 UTC

3.2.2 Vertical Structure

In this section we present the results of the vertical structure of the sea breeze, plotting an east–west cross-section at the GCFV airport weather station. This section is almost perpendicular to the shoreline at Fuerteventura airport (Fig. 2, black solid line). The left plot combines potential temperature (K) and the vertical wind component (dPa s^{-1}) to depict the strong ascent flow associated with the sea-breeze progression, whilst the right plot shows the perpendicular wind component to the coast (m s^{-1}), where a blue shaded area denotes a flow from east to west, an onshore flow for the eastern part of the island. In addition, the circulation vectors are overlain to determine the vertical structure of the flow and the extension of the sea-breeze circulation cell.

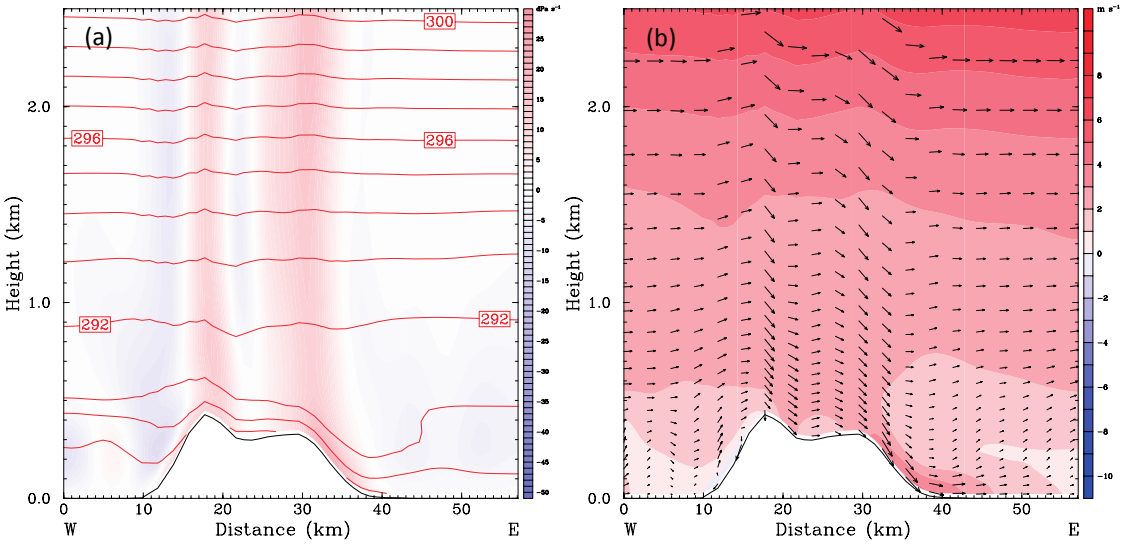

Fig. 9. Cross-section valid for 10 April 2007, 0600 UTC. (a) Potential temperature (K) and vertical wind component (dPa s^{-1}). (b) Perpendicular wind component to the coast (blue contours denote movement from the east to the west) and circulation vectors

The first plots in Fig. 9 are temporally equivalent to those in Fig. 5, depicting the flow in the first 2.5 km above Fuerteventura Island at sunrise, before the onset of the sea-breeze circulation. There is a well-defined low-level flow from the north-west that is almost perpendicular to the orographic barrier. Due to the stability of the upper layers of the atmosphere, the orography of Fuerteventura Island produces a mountain wave pattern (Fig. 9b). Then, the flow accelerates downwind of the ridge in the cross-section. Maximum wind speeds below 1 km height are located along the eastern side of the island in the lee of the mountain range (Fig. 9b), resulting in an offshore flow (>6 m s^{-1}). The maximum wind speed values in Figs. 5–6 (leeward side) are therefore likely to be primarily caused by downslope flow.

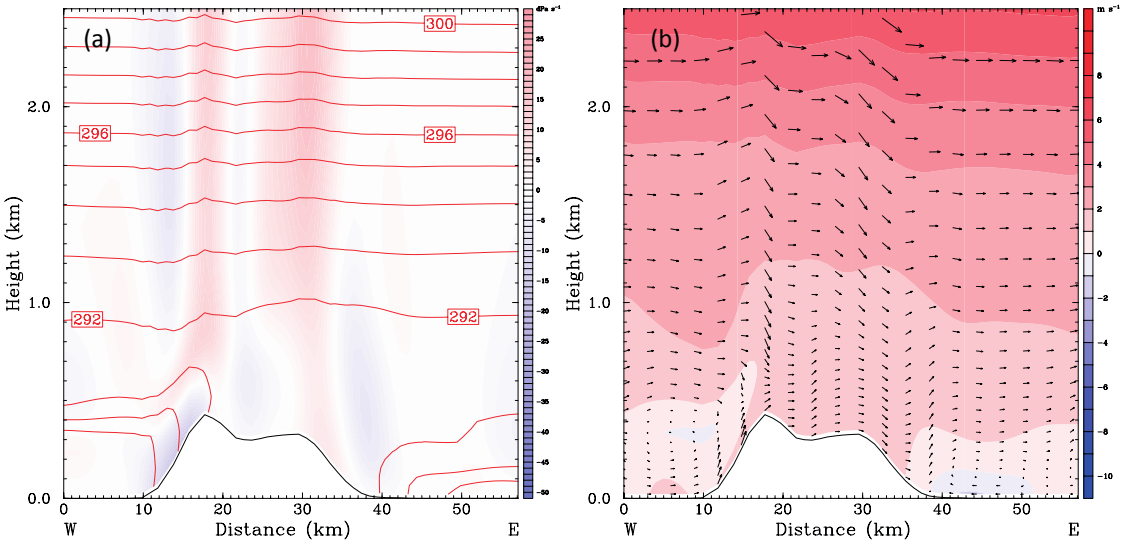

Fig. 10. Same as in Fig. 9, but for 0900 UTC

Three hours after dawn, the eastward flow becomes less intense, especially on the leeward side of the island. The wave pattern associated with the orographic lifting is still visible over 1 km height as well. The upward vertical motion starts at the coast (Fig. 10a), where the onshore flow has developed a sea-breeze cell windward of the island. As expected, the onshore flow favours the formation of the sea-breeze cell but generates a weaker system with a diffuse front (Dailey and Fovell 1999). Figure 10b depicts the onset of the sea breeze at the leeward side, as a blue area appears over the sea, which is close to the eastern coast of Fuerteventura. The beginning of the sea-breeze circulation against the offshore flow is synchronous with the change in wind direction shown in Figs. 4a, 6a, and 6b.

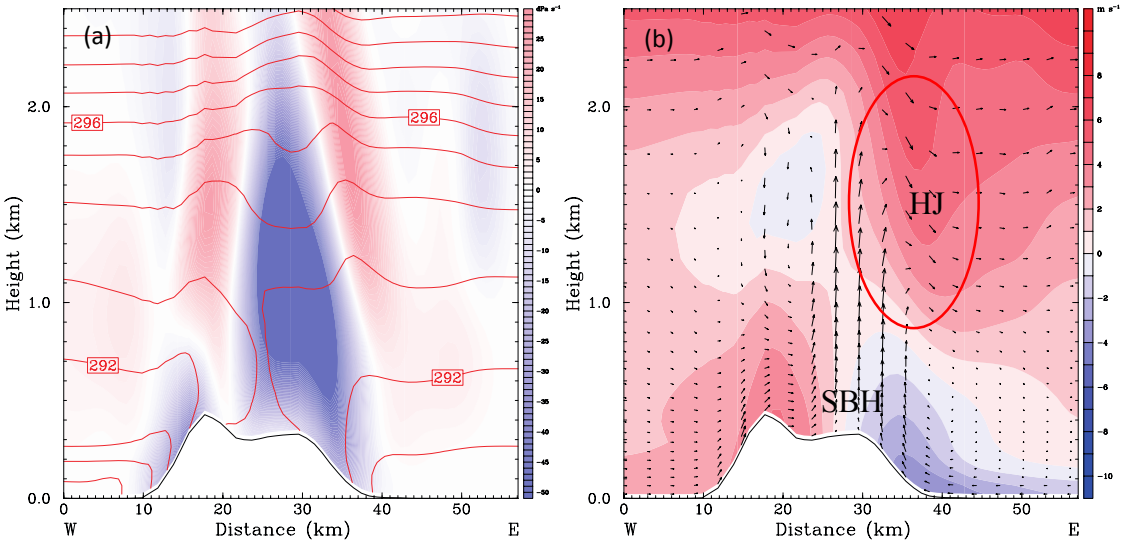

Fig. 11. Same as in Fig. 9, but for 1400 UTC. The hydraulic jump (HJ) and the sea-breeze head (SBH) are marked in Fig. 11 (b)

Figure 11 displays the maximum development of both sea-breeze cells. Figure 11a shows an intense updraft (<-50 dPa s^{-1}) over the island, reaching more than 2 km in height. This updraft is strong enough to start the breaking of the mountain waves, turning the upper flow into a hydraulic jump in the lee (Kirshbaum et al. 2018). Figure 11b illustrates that the sea-breeze circulation reaches more than 10 km inland for both cells, where the sea-breeze head reaches twice the height of the feeder flow, featuring the characteristic shape of an SBF (Dailey and Fovell 1999; Crosman and Horel 2010). This situation is almost identical to that described by the numerical simulation of Wang and Kirshbaum (2017), including the approximate hour of the collision of both SBF, even when the shape of the mountain barrier and the latitude are not exactly the same (Fuerteventura Island is steeper). The trade-wind inversion is located at this moment at about 2,586 m (Fig. 3) together with the hydraulic jump aloft the sea-breeze head. The trade-wind inversion, which is usually found at lower levels (Carrillo et al. 2016) prevents the development of deep convection, and only shallow convection may be expected unless trade-wind inversion weakens or even disappears. The development of the leeward sea-breeze cell, which moves against an offshore flow, reaches its maximum at 1400 UTC. This is congruent with previous theoretical studies regarding the evolution of sea breezes and the development of convection (Dailey and Fovell 1999; Fovell 2005; Wang and Kirshbaum 2017).

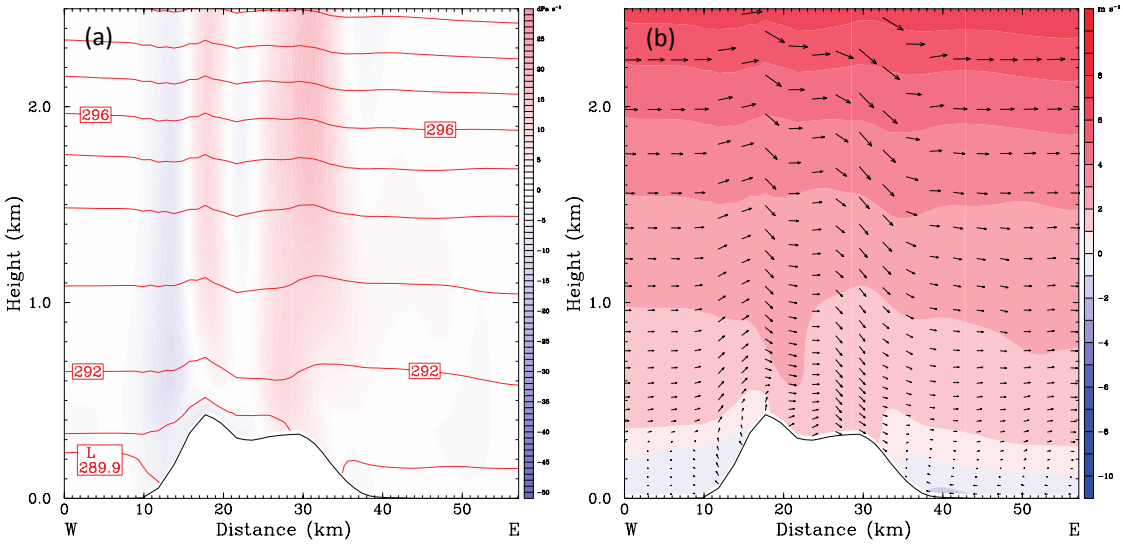

Fig. 12. Same as in Fig. 9, but for 2100 UTC

Finally, Fig. 12 illustrates how the prevailing pressure-driven wind direction overwhelms the sea-breeze circulation about two hours after sunset. The PBL becomes less convective (Fig. 12a), with almost no areas of upward motion except for on the windward side of the island, where the vertical flow is clearly dominated by orographic lifting. Figure 12b characterizes the prevailing background flow where the wave pattern above the island is developing again, similar to prior to the onset of the sea breeze, with no sea-breeze cell or inland flow.

4. Conclusions

We use numerical simulations to investigate sea breezes and their evolution along the eastern boundary of the subtropical North Atlantic at Fuerteventura Island, Canaries archipelago, Spain. We chose three local and two non-local closure PBL schemes, widely used in WRF model simulations, which have been chosen for testing in similar conditions. The simulated outputs were compared with observational data provided by several meteorological stations from the shore to the centre of Fuerteventura, in order to find the best choice for PBL parametrization and its coupling with the surface-layer scheme.

The results for the 10-m wind simulation show a good agreement for the ground station close to the shore, but lower accuracy for those stations near locations with a more complex topography. However, the results for 2-m temperature revealed a very strong correlation between simulated and observed temperatures for all of the meteorological stations. Our tests indicate that non-local closure schemes are the best options and the

YSU PBL scheme coupled with the Revised MM5 similarity surface-layer scheme is optimal. This option is in agreement with Arrillaga et al. (2016), Huang et al. (2016), Dandou et al. (2017), and Calmet et al. (2018).

The day starts with a north-westerly offshore flow along the leeward coast of Fuerteventura Island, which delays the onset of the sea breeze to three hours after sunrise but facilitates the initiation of the sea-breeze cell windward. Once the wind direction starts to turn due to the reversed lee-side flow, the sea-breeze cell is formed leeward, including both veering (along the north-east coast) and backing (south-east coast). The leeward SBF progresses inland, reaching the central part of the island about three hours later. These opposing wind directions create an upward flow close to the central ridge, triggering a shallow convection episode. This strong upward vertical motion collides with the hydraulic jump in the upper levels, which, together with the trade-wind inversion, limits the vertical extension of the convective cell. Finally, as the land starts to cool, the sea-breeze cell diminishes and is overwhelmed by the prevalent pressure-driven flow from the north-west once again, with a return to pre-event conditions about three hours after sunset.

The results of this case study necessitate further refinement of the model, including a finer domain and an updated soil composition and vegetation (as suggested by Calmet et al. 2018) owing to the rapid growth of the population of Fuerteventura Island since 2007. Today, urban areas extend all along the leeward coast, resulting in a new soil pattern. This will not only facilitate the reproduction of finer-scale structures (such as convective rolls) but also exploration of their interaction with the sea breeze. Furthermore, following Lombardo et al. (2018), it would be worthwhile testing the impact of spatial variation in initial sea temperature for this subtropical region. Lastly, future updating of the meteorological station network will improve our knowledge of this phenomenon on the island of Fuerteventura.

Acknowledgements. This article is a publication of the Unidad Océano y Clima of the Universidad de Las Palmas de Gran Canaria, a R&D&i CSIC- associate unit. This research has been supported by RIS-3 PO Feder Canarias through project BOUNDARY (ProID2017010083). All plots where created by NCAR Command Language (NCL)[3]. The authors also thank the anonymous reviewers for their insightful comments, which helped to improve this article.

[3] The NCAR Command Language (Version 6.6.2) [Software]. 2019. Boulder, Colorado: UCAR/NCAR/CISL/TDD. http://dx.doi.org/10.5065/D6WD3XH5

Appendix

Table 5 Mathematical formulations of the statistical indexes used for wind speed, wind direction and 2-m temperature

Index	Formula
MBE	$MBE = \bar{S} - \bar{O}$
RMSE	$RMSE = \left[\frac{1}{n}\sum_{i=1}^{n}(S_i - O_i)^2\right]^{\frac{1}{2}}$
ρ	$\rho = \frac{\sum_{1=1}^{n}(S_i - \bar{S})\,(O_i - \bar{O})}{\sqrt{\sum_{i=1}^{n}(S_i - \bar{S})^2}\sqrt{\sum_{i=1}^{n}(O_i - \bar{O})^2}}$
IA	$IA = 1 - \frac{\sum_{i=1}^{n}(S_i - O_i)^2}{\sum_{i=1}^{n}(\lvert S_i - \bar{O}\rvert + \lvert O_i - \bar{O}\rvert)^2}$

S stands for the modelled and O the observed value of each parameter, paired in space and time for each *i* of the *n* data pairs. The overbar indicates mean value and n is the sample size

References

Arrillaga JA, Yagüe C, Sastre M, Román-Cascón C (2016) A characterisation of sea-breeze events in the eastern Cantabrian coast (Spain) from observational data and WRF simulations. Atmos Res 181:265–280

Azorin-Molina C, Tijm S, Ebert EE, Vicente-Serrano S-M, Estrela M-J (2015) High resolution HIRLAM simulations of the role of low-level sea-breeze convergence in initiating deep moist convection in the eastern Iberian Peninsula. Boundary-Layer Meteorol 154:81–100

Banks RF, Tiana-Alsina J, Baldasano JM, Rocadenbosch F, Papayannis A, Solomos S, Tzanis CG (2016) Sensitivity of boundary-layer variables to PBL schemes in the WRF model based on surface meteorological observations, lidar, and radiosondes during the HygrA-CD campaign. Atmos Res 176–177:185–201

Buckley RL, Weber AH, Weber JH (2004) Statistical comparison of Regional Atmospheric Modelling System forecast with observations. Meteorol Appl 11: 67-82

Calmet I, Mestayer PG, Van Eijk AMJ, Herlédant O (2018) A coastal bay summer breeze study, part 2: high-resolution numerical simulation of sea-breeze local influences. Boundary-Layer Meteorol 167:27–51

572 Carrillo J, Guerra JC, Cuevas E, Barrancos J (2016) Characterization of the marine boundary layer and the
573 trade-wind inversion over the sub-tropical North Atlantic. Boundary-Layer Meteorol 158:311–330

574 Chen F, Dudhia J (2001) Coupling an advanced land surface–hydrology model with the Penn State–NCAR
575 MM5 modeling system. Part II: preliminary model validation. Mon Weather Rev 129:587–604

576 Cohen AE, Cavallo SM, Coniglio MC, Brooks HE (2015) A review of planetary boundary layer
577 parameterization schemes and their sensitivity in simulating southeastern U.S. cold season severe
578 weather environments. Weather Forecast 30:591–612

579 Crosman ET, Horel JD (2010) Sea and lake breezes: a review of numerical studies. Boundary-Layer
580 Meteorol 137:1–29

581 Dailey PS, Fovell RG (1999) Numerical simulation of the interaction between the sea-breeze front and
582 horizontal convective rolls. Part I: offshore ambient flow. Mon Weather Rev 127:858–878

583 Dalu GA, Pielke RA (1989) An analytical study of the sea breeze. J Atmos Sci 46:1815–1825

584 Dandou A, Tombrou M, Kalogiros J, Bossioli E, Biskos G, Mihalopoulos N, Coe H (2017) Investigation
585 of turbulence parametrization schemes with reference to the atmospheric boundary layer over the
586 Aegean Sea during etesian winds. Boundary-Layer Meteorol 164:303–329

587 Dimitrova R, Silver Z, Zsedrovits T, Hocut CM, Leo LS, Di Sabatino S, Fernando HJS (2016) Assessment
588 of planetary boundary-layer schemes in the Weather Research and Forecasting Mesoscale Model using
589 MATERHORN field data. Boundary-Layer Meteorol 159:589–609

590 Ferrero E, Alessandrini S, Vandenberghe F (2018) Assessment of planetary-boundary-layer schemes in the
591 Weather Research and Forecasting Model within and above an urban canopy layer. Boundary-Layer
592 Meteorol 168:289–319

593 Fovell RG (2005) Convective initiation ahead of the sea-breeze front. Mon Weather Rev 133:264–278

594 Fovell RG, Dailey PS (2001) Numerical simulation of the interaction between the sea-breeze front and
595 horizontal convective rolls. Part II: alongshore ambient flow. Mon Weather Rev 129:2057–2072

596 Garratt J (1990) The internal boundary layer—a review. Boundary-Layer Meteorol 50:171-203

597 Gibbs JA, Fedorovich E, Van Eijk AMJ (2011) Evaluating weather research and forecasting (WRF) model
598 predictions of turbulent flow parameters in a dry convective boundary layer. J Appl Meteorol Climatol
599 50:2429–2444

600 Gilliam RC, Pleim JE (2010) Performance assessment of new land surface and planetary boundary layer
601 physics in the WRF-ARW. J Appl Meteorol Climatol 49:760–774

Grell GA, Dévényi D (2002) A generalized approach to parameterizing convection combining ensemble and data assimilation techniques. Geophys Res Lett 29:38–1–38–4

Grenier H, Bretherton CS (2001) A moist PBL parameterization for large-scale models and its application to subtropical cloud-topped marine boundary layers. Mon Weather Rev 129:357–377

Gunwani P, Mohan M (2017) Sensitivity of WRF model estimates to various PBL parameterizations in different climatic zones over India. Atmos Res 194:43–65

Hernández-Guerra A, Machín F, Antoranz A, Cisneros-Aguirre J, Gordo C, Marrero-Díaz A, Martínez A, Ratsimandresey A-W, Rodríguez-Santana A, Sangrá P, López-Laazen F, Parrilla G. Pelegrí JL (2002) Temporal variability of mass transport in the Canary Current. Deep Sea Res II 49:3415-3426

Hong S-Y, Noh Y, Dudhia J (2006) A new vertical diffusion package with an explicit treatment of entrainment processes. Mon Weather Rev 134:2318–2341

Huang H-Y, Hall A, Teixeira J (2013) Evaluation of the WRF PBL parameterizations for marine boundary layer clouds: cumulus and stratocumulus. Mon Weather Rev 141:2265–2271

Huang Q-Q, Cai X-H, Song Y, Kang L (2016) A numerical study of sea breeze and spatiotemporal variation in the coastal atmospheric boundary layer at Hainan Island, China. Boundary-Layer Meteorol 161:543–560

Hughes CP, Veron DE (2018) A characterization of the Delaware sea breeze using observations and modeling. J Appl Meteorol Climatol 57:1405–1421

Janjić ZI (1994) The step-mountain eta coordinate model: further developments of the convection, viscous sublayer and turbulence closure schemes. Mon Weather Rev 122:927–945

Jiménez PA, Dudhia J, González-Rouco JF, Navarro J, Montávez JP, García-Bustamante E (2012) A revised scheme for the WRF surface layer formulation. Mon Weather Rev 140:898–918

Jousse A, Hall A, Sun F, Teixeira J (2016) Causes of WRF surface energy fluxes biases in a stratocumulus region. Climate Dynamics 46:571–584

Kirshbaum DJ, Adler B, Kalthoff N, Barthlott C, Serafin S (2018) Moist orographic convection: physical mechanisms and links to surface-exchange processes. Atmosphere 9,80:1-26

Kwun JH, Kim Y-K, Seo J-W, Jeong JH, You SH (2009) Sensitivity of MM5 and WRF mesoscale model predictions of surface winds in a typhoon to planetary boundary layer parameterizations. Natural Hazards 51:63–77

Lin Y-L, Farley RD, Orville HD (1983) Bulk parameterization of the snow field in a cloud model. J Clim Appl Meteorol 22:1065–1092

633 Lombardo K, Sinsky E, Edson J, Whitney MM, Jia Y (2018) Sensitivity of offshore surface fluxes and sea
634 breezes to the spatial distribution of sea-surface temperature. Boundary-Layer Meteorol 166:475–502

635 Miller STK, Keim BD, Talbot RW, Mao H (2003) Sea breeze: structure, forecasting, and impacts. Rev
636 Geophys 41:1–31

637 Mlawer EJ, Taubman SJ, Brown PD, Iacono MJ, Clough SA (1997) Radiative transfer for inhomogeneous
638 atmospheres: RRTM, a validated correlated-k model for the longwave. J Geophys Res Atmos
639 102:16663–16682

640 Nakanishi M, Niino H (2006) An improved Mellor-Yamada Level-3 model: its numerical stability and
641 application to a regional prediction of advection fog. Boundary-Layer Meteorol 119:397–407

642 Nunalee C, Basu S (2014) Wind energy - impact of turbulence. Research Topics in Wind Energy 2:197–
643 202

644 Pleim JE (2007) A combined local and nonlocal closure model for the atmospheric boundary layer. Part I:
645 model description and testing. J Appl Meteorol Climatol 46:1383–1395

646 Pleim JE, Xiu A (1995) Development and testing of a surface flux and planetary boundary layer model for
647 application in mesoscale models. J Appl Meteorol 34:16–32

648 Qian T, Epifanio CC, Zhang F (2012) Topographic effects on the tropical land and sea breeze. J Atmos Sci
649 69:130–149

650 Rotunno R (1983) On the linear theory of the land and sea breeze. J Atmos Sci 40:1999–2009

651 Skamarock WC, Klemp JB, Dudhia J, Gill DO, Barker DM, Duda M, Huang X-Y, Wang W, Powers JG
652 (2008) A description of the advanced research WRF version 3. NCAR Technical Note, NCAR/TN-
653 468+STR

654 Smith EN, Gibbs JA, Fedorovich E, Klein P (2018) WRF Model Study of the Great Plains Low-Level Jet:
655 Effects of Grid Spacing and Boundary Layer Parameterization. J Appl Meteorol 57:2375–2397

656 Smolarkievicz PK, Rassmussen RM, Clark TL (1988) On the dynamics of Hawaiian cloud bands: Island
657 forcing. J Atmos Sci 45:1872-1905

658 Soderholm B, Ronalds B, Kirshbaum DJ (2014) The evolution of convective storms initiated by an isolated
659 mountain ridge. Mon Weather Rev 142:1430-1451

660 Soriano C, Jorba O, Baldasano JM (2004) One-Way Nesting Versus Two-Way Nesting: Does It Really
661 Make a Difference? In: Borrego C., Schayes G. (eds) Air Pollution Modeling and Its Application XV.
662 Springer, Boston, MA

663 Stull RB (1991) Static stability—an update. Bull Am Meteorol Soc 72:1521–1529

664 Tymvios F, Charalambous D, Michaelides S, Lelieveld J (2018) Intercomparison of boundary layer
665 parameterizations for summer conditions in the eastern Mediterranean island of Cyprus using the WRF
666 - ARW model. Atmos Res 208:45–59

667 Wang CC, Kirshbaum DJ (2015) Thermally forced convection over a mountainous tropical island. J Atmos
668 Sci 72:2484-2506

669 Wang CC, Kirshbaum DJ (2017) Idealized simulations of sea breezes over mountainous islands. Q J R
670 Meteorol Soc 143:1657-1669

671 Xian Z, Pielke RA (1991) The effects of width of landmasses on the development of sea breezes. J Appl
672 Meteorol 30:1280–1304

673 Yver CE, Graven HD, Lucas DD, Cameron-Smith PJ, Keeling RF, Weiss RF (2013) Evaluating transport
674 in the WRF model along the California coast. Atmos Chem Phys 13:1837–1852